Effect of annealing temperature on morphologies of metal organic framework derived NiFe$_2$O$_4$ for supercapacitor application

P.D. Patil [a], S.R. Shingte [b], V.C. Karade [c], J.H. Kim [c], T.D. Dongale [a], S.H. Mujawar [d], A.M. Patil [e], P.B. Patil [b,*]

[a] School of Nanoscience and Technology, Shivaji University, Kolhapur, Maharashtra, 416004, India
[b] Department of Physics, The New College, Shivaji University, Kolhapur, Maharashtra, 416012, India
[c] Optoelectronic Convergence Research Center and Department of Materials Science and Engineering, Chonnam National University, Gwangju 500757, South Korea
[d] Department of Physics, Yashawantrao Chavan Institute of Science, Satara, Maharashtra, 415001, India
[e] Department of Mechanical Engineering, Yonsei University 50 Yonsei-ro, Sinchon-dong, Seodaemun-gu, Seoul, South Korea

A R T I C L E   I N F O

A B S T R A C T

The aim of this work is to obtain different morphologies of the metal organic framework (MOF) derived NiFe$_2$O$_4$ (NFO) for supercapacitor application. The NFO samples were obtained by annealing solvothermaly synthesized NiFe$_2$ MOF. The crystalline phase, morphology, particle size, and presence of functional groups of NFO were investigated by X-ray diffractometry (XRD), Scanning electron microscopy (SEM), Transmission electron microscopy (TEM), and Fourier transform infrared spectroscopy (FTIR), respectively. Moreover, chemical states, surface area, and pore size distribution of the optimized sample are evaluated by X-ray photoelectron spectroscopy (XPS) and surface area analyzer, respectively. The cubic spinel structured MOF derived NFO with different morphologies like threads, mesh-like structure, and grains were obtained at annealing temperatures of 460 °C, 500 °C, and 550 °C, respectively. FTIR analysis revealed the organic ligands decomposes with increasing annealing temperature. XPS analysis showed that MOF derived NFO prepared by annealing at 500 °C (NFO500) has Ni^{2+}, Fe^{2+}, and Fe^{3+} states with some NiO impurities. Sharp edged rhombus nanoplates with interconnected mesh-like structure was observed for MOF derived NFO500. The synthesized MOF derived NFO500 electrode showed a mesoporous nature with a specific surface area of 38.17 m^2 g^{-1}, which can be favourable for efficient charge transfer and high energy storage capability. The MOF derived NFO500 electrode exhibited a high specific capacitance of 833 F g^{-1} and specific energy of 42 Wh kg^{-1} at a specific power of 154 W kg^{-1} in 1 M KOH. After 3000 continuous cycles, NFO500 retained 74% capacitance at 3 A g^{-1} with 84% coulombic efficiency. The good electrochemical performance of MOF derived NFO500 compared to other samples is attributed to the mesh-like structure facilitating the diffusion of OH$^-$ ions into the electrode and the low charge-transfer resistance (2.7 Ω cm^{-2}) between electrode and electrolyte interface. This study highlights the utility of modifying the morphologies of MOF derived nanostructures for energy storage applications.

1. Introduction

Electrochemical supercapacitors are energy storage devices that bridge the gap between batteries and capacitors [1]. It has a vast market in both portable devices and hybrid electric vehicles to improve energy recovery by fast charge and fast discharge capability [2]. Supercapacitors are classified as electrochemical double-layer capacitors (EDLCs) and pseudocapacitors, depending on their charge storage mechanism. EDLCs possess physical charge separation by ion adsorption at the electrode-electrolyte interface, while pseudocapacitors chemically store the charges by fast reversible faradic redox reactions on or near the electrode surface [3]. EDLCs type supercapacitors are based on carbon and carbon derived materials. On the other hand, pseudocapacitors are generally made up of transition metal oxides (TMOs), hydroxides, sulfides, nitrides, and conductive polymers. While hybrid supercapacitors (HSCs) contain one electrode of EDLC type and the other is of battery or pseudocapacitive type [4]. Among the various materials for energy storage systems, TMOs with spinel structure

---

(denoted as $A_xB_{3-x}O_4$ where A, B = Co, Zn, Ni, Fe, Cu, Mn, etc.) are immerged as an attractive electrode material due to its low cost, easy synthesis, high electrochemical activity, stability, and easy control of morphologies [5]. Among all the TMOs, nickel-based materials have been intensively investigated and considered as good potential electrode materials for pseudocapacitors due to their high specific capacitance [6], high chemical and thermal stability, and lower cost [7, 8]. Binary TMOs, such as different ferrites, particularly $MnFe_2O_4$ [9], $CoFe_2O_4$ [3], and $NiFe_2O_4$ [10] exhibits higher capacitance. TMOs are attractive for supercapacitor application because they provide multiple redox species and exhibit higher electrical conductivity due to relatively low activation energy or electron transfer between the metal cations [11]. Although TMOs possess high capacitance, their utilization of multiple redox sites results in a low cycle life [12]. TMOs with controlled nanoporous architectures with a high surface area are essential to achieve the desired electrochemical performance. Metal organic frameworks (MOFs) are porous materials with metal ions coordinated to organic linkers. The unique chemical constitution of MOFs allows the formation of diverse microstructures and properties which are intensively utilized for varity of application [11]. Liao et al. engineered a Au-Pd alloy nanoparticles-doped cobalt oxide interface derived from metal organic frameworks for selective oxidation of 5-hydroxymethylfurfural to 2, 5-furandicarboxylic acid [13]. They have also reviewed the utilization of MOF derived materials as effective solid catalysts for the valorization of biomass into platform chemicals [14]. Liu et al. achieved ultrahigh selective and ultrafast osmotic transport in ion channel-mimetic MOF based membranes explored advanced separation technologies and energy-harvesting devices [15]. The MOFs and MOF derived materials receive growing attention for fine chemical synthesis due to their versatile tunability and high catalytic activity. Further, the MOF derived materials allow high controllability in the design of catalyst systems for organic reactions. Konnerth et al. reviewed design and synthesis conditions to obtain highly active MOF derived catalysts [16].

MOFs are becoming popular as a precursor or template for the preparation of TMOs with a high specific surface area, controllable structure, and adjustable pore size [11, 17]. Such MOF derived TMOs provide effective transportation paths for enhanced kinetics of electroactive species and fast diffusion of electrolyte ions to achieve superior electrochemical performance [5]. The iron-based MOF derived TMOs exhibits higher electrical conductivity and significantly smaller charge activation energies across MOF derived TMO families. It possesses the Fe^{2+} and the $Fe^{3+/2+}$ mixed valencies, which help to improve electrical conductivity [18]. Metal oxide composites derived from MOFs with diverse morphologies are excellent electrode materials due to their high capacitance, superior rate performance [19]. Mahmood et al. reported a symmetric supercapacitor based on nanostructured MOF derived $Fe_3O_4/Fe/C$ hybrid with a specific capacitance of 600 F g^{-1} at a current density of 1 A g^{-1} [20]. Chen et al. reported the novel nickel based MOF as electrode material for supercapacitor. The MOF derived mixed TMOs such as $NiFe_2O_4$, $ZnFe_2O_4$, and $CoFe_2O_4$ have been reported with specific capacities of 636, 449, and 380 mAh g^{-1}, respectively, at a high current density of 8.0 A g^{-1} [21].

However, the wide applications of MOF derived materials as an electrode are still limited due to their relatively low conductivity and instability in electrolytes which can be partly compensated by structural optimization [22]. To achieve an enhancement in electrochemical performance, it is desirable to explore diverse MOF morphologies with the deliberate control of structure, and therefore the properties and function [23]. Many effective systems have been developed to investigate the effect of surface properties like pore size and surface area of MOF on their charge storage capacity [23]. Among all of them, varying annealing temperatures is more intensively followed [24]. The annealing temperature has a strong impact on the surface area and porosity of the material, which plays a vital role in the sensing [25] and electrochemical devices [26]. Wu et al. reported MOF derived hollow double-shelled NiO nanospheres with different calcination temperatures. The NiO

calcinated at 400 °C owns a high surface area with abundant channels for diffusion of OH$^-$ ions. It showed the specific capacitance of 473 F g^{-1} at the current density of 0.5 A g^{-1} with 94% capacitance retention after 3000 cycles [26]. Chen et al. reported $ZnCo_2O_4$ using mixed MOF (Zn-Co-MOF) for supercapacitor via calcining in the air at 400 °C, 450 °C, and 500 °C. The specific capacitance of 457 F g^{-1} at the current density of 1 A g^{-1} was obtained at 400 °C due to the large surface area. After 1500 cycles, the specific capacitances remained at about 425 F g^{-1} (97.9 %), at current density 2 A g^{-1} [27].

We present a study on the structural and morphological evolution of MOF derived nickel ferrite ($NiFe_2O_4$) through controlled annealing. By varying the annealing temperature, three morphologies were obtained: 1) interwoven threads, 2) mesh-like morphology, and 3) grains (spheres). The electrochemical performance of these materials as a supercapacitor electrode was evaluated.

2. Materials and method

2.1. Materials

All the chemicals were of analytical grade, purchased from commercial sources and used without further purification. Iron (III) chloride hexahydrate ($FeCl_3 \bullet 6H_2O$) and terephthalic acid (H_2BDC) were procured from Sigma-Aldrich. Nickel (II) nitrate hexahydrate (Ni $(NO_3)_2 \bullet 6H_2O$) and N, N–Dimethylformamide (DMF) were purchased from SRL. Sodium hydroxide pellets (NaOH) were purchased from Loba Chemie Pvt. Ltd.

2.2. Synthesis of MOF derived $NiFe_2O_4$

Initially, $NiFe_2$ MOF was prepared by the solvothermal method. For this, nickel nitrate hexahydrate (3.3 mM) and ferric chloride hexahydrate (6.7 mM) were dissolved in 10 ml DMF. The solution of terephthalic acid (9.9 mM) in 10 ml of DMF was added to the above mixture and stirred continuously to obtain a homogeneous solution. The precipitation was achieved by dropwise addition of NaOH (400 mM) in the solution. The precipitate was then transferred into a 25 ml Teflon-lined autoclave and kept at 100 °C for 15 h. Finally, the sample was washed several times with DMF and distilled water and dried at 60 °C for 2 h. The annealing of the prepared samples was carried out in two steps, initially at 100 °C for 2 h. Then the samples were annealed at 460 °C, 500 °C, and 550 °C for 6 h and naturally cooled samples of MOF derived $NiFe_2O_4$ powder were labelled as NFO460, NFO500, and NFO550, respectively.

2.3. Preparation of working electrode

Stainless Steel (SS) substrates (1 × 3 cm^2) were polished with polish paper until the mirror shine surface was obtained and sonicated in ethanol for 15 min. The working electrodes were prepared by mixing the MOF derived $NiFe_2O_4$, polyvinyl difluoride, and activated carbon in a weight ratio of 80:10:10. The mixture was ground in an agate mortar to form a homogenous slurry by adding adequate drops of N-Methyl-2-pyrrolidone. The doctor blade technique was employed to deposit the paste on the cleaned SS substrates. These films were then kept at 60 °C for 12 h for drying.

2.4. Characterizations

The crystallinity and phase of the samples were studied by X-ray diffractometry (XRD Ultima IV, Rigaku Corporation, Japan) with Cu K$_\alpha$ radiation (λ=1.5406 Å). To analyze the presence of functional groups, Fourier transform infrared (FTIR, Jasco spectrometer) spectra were recorded in the range 4000–400 cm^{-1}. To study the morphology of synthesized materials, scanning electron microscopy (SEM, JEOL JSM-IT 200) was employed. The contact angle of materials was measured

using a contact angle meter (Holmarc optomechanics Pvt. Ltd). The elemental and surface chemistry of elements were investigated by X-ray photoelectron spectroscopy (XPS, Thermo VG Scientific, UK) with a monochromatic Mg Kα (1253.6 eV) radiation source. Morphology and particle size were investigated using a transmission electron microscopy (TEM, Tecnai G2 S-Twin). The surface area and pore size distribution of electrode material were evaluated using a Quantachrome Instruments v10.0 surface area analyzer.

2.5. Electrochemical measurements

To study the supercapacitive performance, the conventional three-electrode configuration was assembled using $NiFe_2O_4$ films as a working electrode, platinum (Pt) wire as a counter electrode, and Ag/AgCl as a reference electrode. The 1 M KOH aqueous solution was used as an electrolyte. Electrochemical measurements such as cyclic voltammetry (CV), electrochemical impedance spectroscopy (EIS), and galvanostatic charge-discharge (GCD) were carried out using Metrohm Autolab PGSTAT204 electrochemical workstation.

3. Results and discussion

3.1. Characterization of MOF derived $NiFe_2O_4$

XRD analysis was carried out to investigate the phase and crystallite size of the synthesized MOF derived $NiFe_2O_4$ samples. As shown in **Fig. 1**A, for all the samples, the diffraction peaks are well indexed with the JCPDS file No-00–010–0325. The peaks indexed at 2θ values 18.4, 30.3, 35.7, 37.3, 43.3, 53.8, 57.3, and 63.0° correspond to lattice planes of (111), (220), (311), (222), (400), (422), (511), and (440) of the cubic spinel structure of the $NiFe_2O_4$. It is observed that the diffraction peaks become narrower and sharper with the increase in annealing temperature, which suggests the enhanced crystallinity in NFO500 and NFO550 samples compared to NFO460. The average crystallite size of the NFO460 and NFO550 samples calculated using (311) peak is found to be 20 and 23 nm, respectively. Surprisingly, NFO500 displays a small crystallite size of 16 nm. The increase in average crystallite size during the annealing process is due to the minimization of the interfacial surface energy [28]. Furthermore, the increase in temperature reduces interparticle distance, resulting in larger grain size particles (Ostwald ripening) [29]. However, the reduction in the crystallite size of NFO500 is due to the massive loss of organic contents and contraction during annealing [30].

The FTIR analysis of the $NiFe_2$ MOF and MOF derived NFO460, NFO500, and NFO550 was carried out to study the presence of

functional groups (**Fig. 1**B). The strong absorption band at 3425 cm^{-1} in all spectra is due to the stretching vibration of the O—H group of adsorbed water molecules from solvent [31]. In the spectrum of $NiFe_2$ MOF (**Fig. 1B(a)**), the strong bands at 1578 and 1370 cm^{-1} are ascribed to the asymmetric and symmetric stretching modes of -COO groups, respectively. The separation between these asymmetric and symmetric stretching modes implies that the -COO group of H_2BDC is coordinated to Ni by a bidentate ligand with a polymeric structure $(BDC)_2$—Ni [32]. Strong bands at 746 and 817 cm^{-1} in the $NiFe_2$ MOF spectrum are assigned to absorption peaks of H_2BDC [33]. For NFO460, NFO500, and NFO550 samples the bands corresponding to -COO and H_2BDC are vanishing due to the decomposition of the organic ligand with the increasing annealing temperature. The absorption band around 400 cm^{-1} is corresponding to the Ni-O bond and the bands observed in the range 600–560 cm^{-1} in all the samples are characteristic of the Fe-O vibrations. These bands are attributed to $NiFe_2O_4$ [34]. It is observed that with an increasing annealing temperature, O—H and Fe-O bands linearly change their positions towards the higher wavenumbers. It may be due to particle aggregation [35].

SEM images of MOF derived NFO460, NFO500, and NFO550 samples at two magnifications are shown in **Fig. 2**. As can be seen in **Fig. 2(A and B)**, the NFO460 sample possesses indistinct interwoven thread-like structures. For NFO500, it is observed that the thread diameter has been increased as the temperature was raised and turned into well-grown mesh-like morphology **(Fig. 2(C and D))**. The overall surface of NFO500 is rougher than NFO460 due to the presence of randomly aligned threads, which may create pores in the material [36]. NFO550 exhibits distinct, small, agglomerated grains **(Fig. 2(E and F))**. SEM study suggests that annealing temperature has influenced the shape and morphology of MOF derived NFO material. The smaller mesh-like structure with porous surface morphology of NFO500 could offer more electroactive sites in the electrochemical reactions compared to the other two samples. The interconnected mesh-like structure is favourable for charge storage as it provides fast charge transfer channels on the surface as well as in the bulk of electroactive materials.

The surface wettability study of NFO460, NFO500, and NFO550 samples was carried out by contact angle measurement **(Fig. 2(G-I))**. For the NFO460 sample, water makes an angle of 60º on the surface of the film. Whereas the surface of NFO500 exhibits a decreased contact angle of 34º, indicating enhanced hydrophilic nature. Thus, the sample annealed at 500 ºC can provide a high affinity between electrode and electrolyte ions. On the other hand, for NFO550, the water drop was immediately soaked as soon as it comes in contact with the film surface revealing its hydrophilic nature. Improved wettability of material increases the electrochemical performance of the material due to the ease
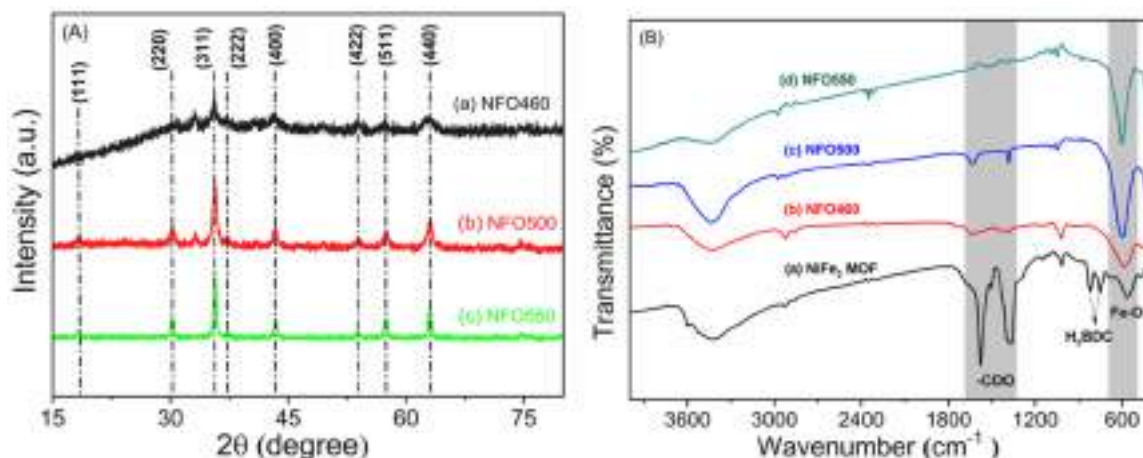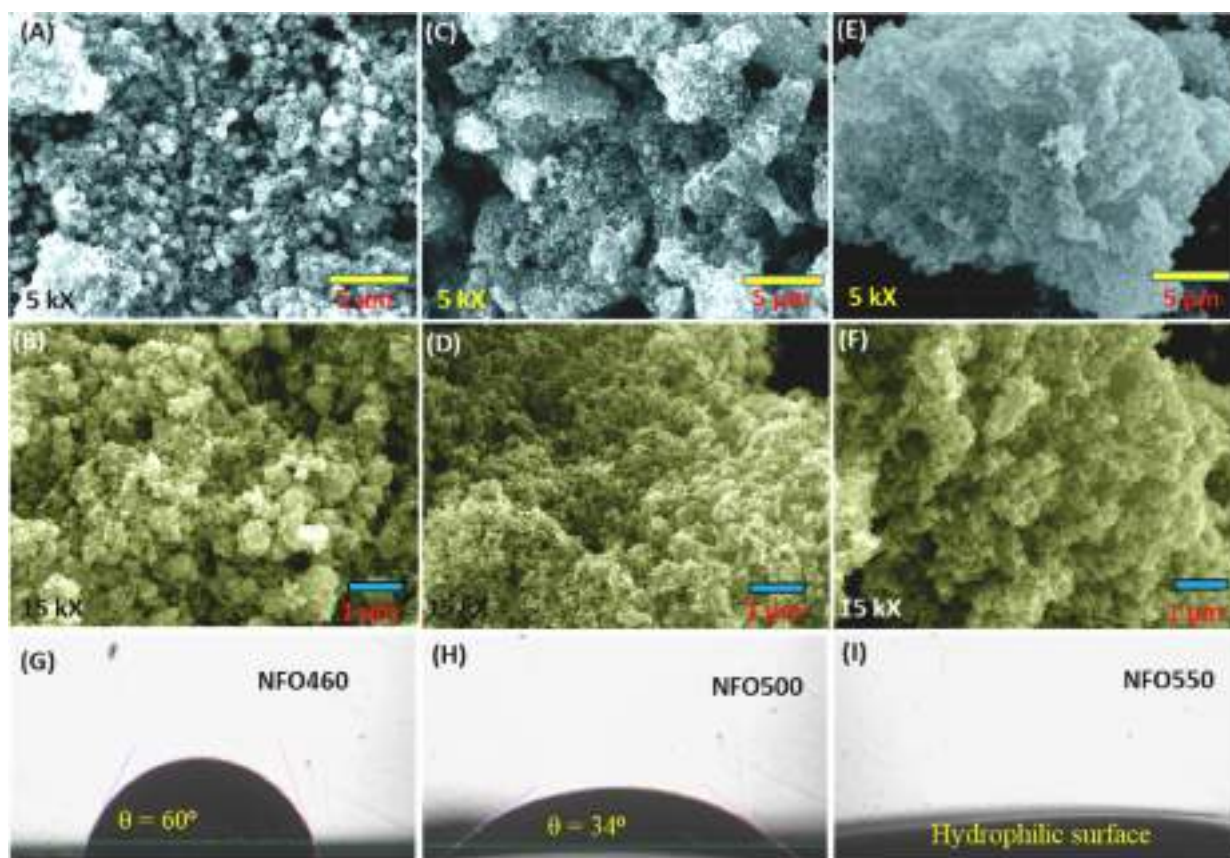

Fig. 1. (A) X-ray diffraction patterns of MOF derived $NiFe_2O_4$ (a) NFO460, (b) NFO500, and (c) NFO550. (B) FTIR spectra of (a) $NiFe_2$ MOF, (b) NFO460, (c) NFO500, and (d) NFO550.

Fig. 2. SEM images of (A and B) NFO460, (C and D) NFO500, and (E and F) NFO550 electrodes at magnifications of 5 kX and 15 kX, respectively, and (G-I) water contact angles measurement photographs of NFO460, NFO500, and NFO550, respectively.

of electrode-electrolyte ion interaction [37].

The chemical states and surface chemistry of elements in the NFO500 were investigated by XPS and high-resolution peaks of Ni 2p, Fe 2p, C 1 s, and O 1 s are shown in Fig. 3. The Ni 2p peak could be deconvoluted into two major binding energy peaks assigned to Ni $2p_{3/2}$ and Ni $2p_{1/2}$ and their corresponding satellites (Fig. 3A). The energy difference (δ eV) between Ni $2p_{3/2}$ and Ni $2p_{1/2}$ peaks are 17.9 eV [38]. The Ni $2p_{3/2}$ peaks centered at 854.6 eV and 856.1 eV correspond to Ni^{2+} (Oh) and Ni^{2+} (Td), respectively. Peaks at 872.1 eV and 873.5 eV resembles with Ni^{2+} (Oh) and Ni^{2+} (Td) of Ni $2p_{1/2}$ [39, 40]. The two major peaks at 856.1 eV and 873.5 eV corresponding to Ni $2p_{3/2}$ and Ni $2p_{1/2}$ are accompanied by two shake-up satellites whose bonding energies are 861.3 and 879.1 eV, respectively. These peaks indicate the presence of Ni^{2+} [41]. The Ni $2p_{3/2}$ spectral lines at 864.8 eV and 867.4 eV are the satellite peaks of NiO [42]. The binding energy peak at 876.4 eV is corresponding to the Ni $2p_{1/2}$ of Ni [43]. The shake-up satellite peak at 881.4 eV is of Ni $2p_{1/2}$, which could be attributed to the oxidation product of Ni on the surface [44]. It is well known that nickel ferrite involves two oxidation states of iron, i.e., Fe^{2+} and Fe^{3+}. Furthermore, both the oxidation states coordinate differently with the oxygen atom, i.e., Fe^{2+} is octahedrally coordinated, whereas Fe^{3+} is tetrahedrally and octahedrally coordinated. Both the binding energy peaks of Fe $2p_{3/2}$ and Fe $2p_{1/2}$ are separated by energy difference (δ eV) of 13.07 eV [38]. As shown in Fig. 3B, the Fe 2p spectrum can be divided into three peaks: one is attributed to Fe^{2+}, while the other two are caused by two lattice sites of Fe^{3+} ions. The binding energy peak of Fe $2p_{3/2}$ comprises of Fe^{2+} and Fe^{3+} (Oh) states at 709.9 eV and 711.2 eV, respectively [39] and the peak at 713.8 eV is assigned to Fe^{2+} [45]. Moreover, the peaks of Fe $2p_{1/2}$ at 723.3 eV, 724.3 eV, and 726.5 eV are associated with Fe^{2+}, Fe^{3+} (Oh), and Fe^{3+} (Td), respectively [39]. The well resolved shake-up satellite peak at 718.7 eV corresponds to Fe $2p_{3/2}$ [46].

The high-resolution XPS spectrum of O 1 s can be separated into two peaks at 531.7 eV and 529.8 eV (Fig. 3C). The peak at a higher binding energy of 531.7 eV is assigned to surface adsorbed hydroxyl (OH^-) groups [47]. On the other hand, the presence of lattice oxygen (O lattice) is confirmed by the peak at the low binding energy of 529.8 eV [48]. Deconvoluted XPS spectrum of C 1 s consists of three peaks at 284.7 eV, 286.1 eV, and 288.4 eV (Fig. 3D), which suggest the presence of carbon or carbon derivatives that could be formed due to the incomplete decomposition of the organic ligand or metal organic framework. The C 1 s spectra can be divided into three individual peaks, where binding energies 284.7 eV, 286.1 eV, and 288.4 eV corresponds to the $C = C$ bond, C—O bond, and the carboxylate carbon (O = C—OH) of the organic ligand terephthalic acid, respectively. [49, 50].

Understanding of the fundamental processes of crystal growth and morphology evolution is important as many of the properties are highly shape and size dependent. Therefore, the morphological study of MOF derived NFO500 was conducted using TEM to gain further insight into structural aspects (Fig. 4(A and B)). The TEM micrographs display sharp edged rhombus shaped nanoplates with a smooth surface. The nanoplates are randomly distributed in structures with an average particle size of 52 nm. The interconnected mesh-like structure can expose the entire and continuous surface area to the electrolyte [51] and also enables intimate contact between particles [52].

The specific surface area and pore size distribution were investigated by N_2 adsorption-desorption measurements. Fig. 5A depicts the N_2 adsorption-desorption isotherm, which demonstrates type IV with an H3-type hysteresis loop, indicating the mesoporous nature of the synthesized material [53, 54]. The Brunauer Emmett Teller (BET) surface area of the NFO500 sample was 38.17 $m^2 g^{-1}$. The mesoporous nature of NFO500 sample with a diameter <15 nm and improved pore volume is reflected in the pore size distribution findings obtained by the
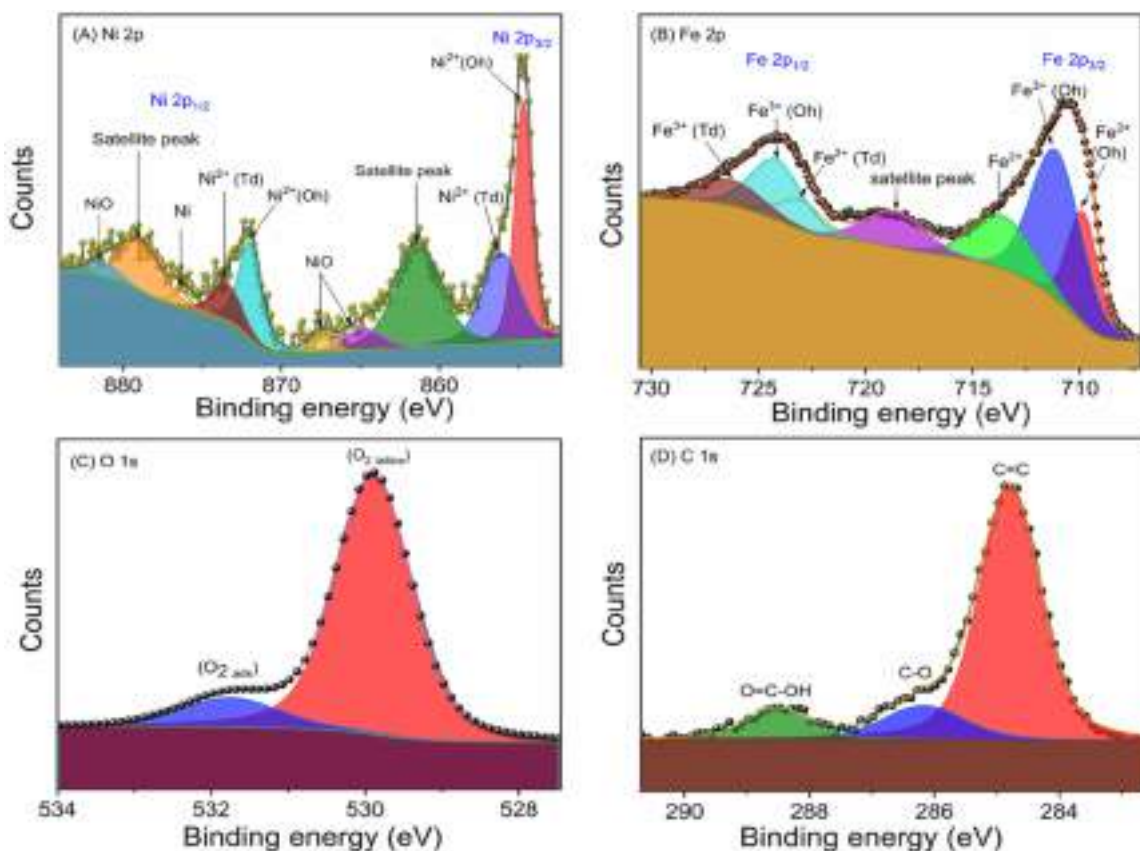
Fig. 3. Deconvoluted XPS spectra of (A) Ni 2p, (B) Fe 2p, (C) O 1 s, and (D) C 1 s of NFO500.
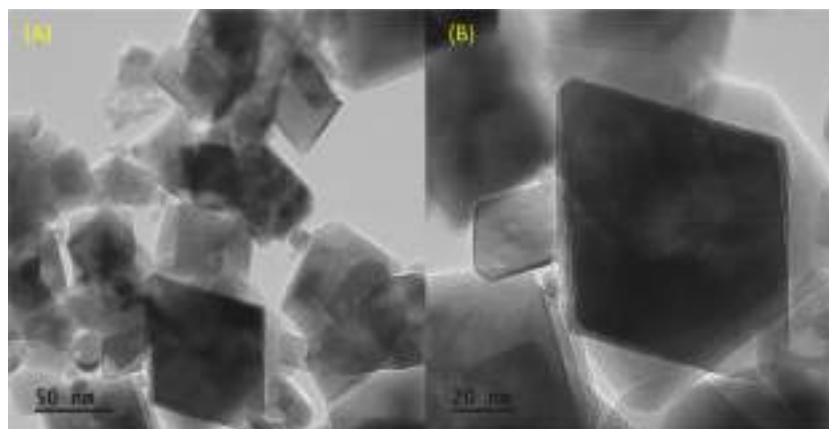

Fig. 4. TEM micrographs of NFO500 at magnifications of (A) 100 kX (B) 200 kX.

Barrett-Joyner-Halenda (BJH) method by applying the nitrogen desorption branch in **Fig. 5**B. The calculated specific surface area and available mesopores are quite favorable for charge transfer and high energy storage. The synthesized NFO500 electrode possesses a sufficient specific surface area and high porosity, which aids in shortening charge transfer pathways and providing more active sites for surface redox reactions which assists to improve the energy storage capability [55]. Furthermore, the mesoporous structure of electrode material can facilitate access to electrolyte ions in the active site's interfacial region, reducing charge transfer paths [56].

3.2. Electrochemical measurements of MOF derived NiFe$_2$O$_4$

The electrochemical behavior of MOF derived NFO460, NFO500, and NFO550 electrodes were studied using cyclic voltammetry in the potential range of -0.1 to 0.5 V in 1 M KOH electrolyte. In **Fig. 6**A, all the three CV curves of these samples have characteristic reduction-oxidation peaks during charging discharging cycles at a scan rate of 50 mV s^{-1}. The redox peaks indicate that the capacitive property is mainly controlled by the faradic redox reactions and hence the investigated MOF material can be considered as a pseudocapacitor [23]. MOF derived NFO500 electrode shows a higher integral area in the CV curve compared to the NFO460 and NFO550 electrodes. Compared to the other two electrodes, the higher peak current and a higher integral area
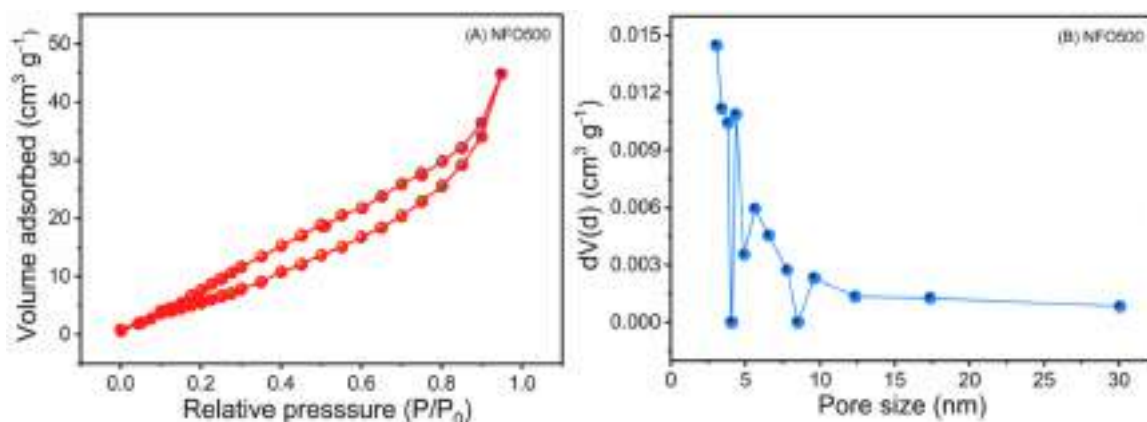
Fig. 5. (A) N_2 adsorption-desorption isotherm and (B) pore size distribution plots of NFO500 electrode material.
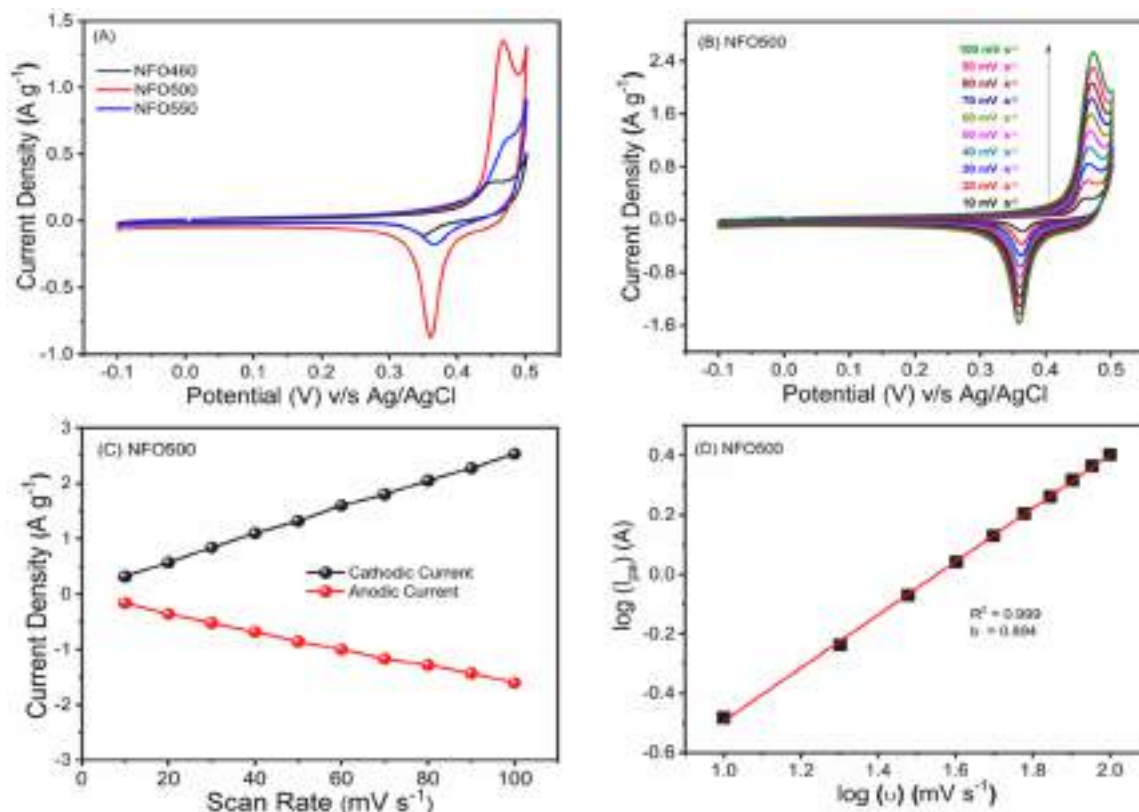

Fig. 6. (A) CV curves of MOF derived NFO460, NFO500, and NFO550 in 1 M KOH at a scan rate of 50 mV s^{-1}. (B) CV curve of MOF derived NFO500 in 1 M KOH at 10–100 mV s^{-1} scan rate. (C) cathodic and anodic current density versus scan rate plots of NFO500 electrode. (D) The plot of log (I_{pa}) v/s log (ν) for the NFO500 sample.

of the MOF derived NFO500 electrode demonstrates that it has better electrochemical reaction activity and higher capacitive performance [57]. The CV measurements of MOF derived NFO500 are carried out in the range of potential −0.1 to 0.5 V at a scan rate of 10–100 mV s^{-1} **(Fig. 6B)**. Redox peak pair in the anodic and cathodic sweeps found in all the CV curves at different scan rates suggest a typical pseudocapacitive nature [58]. However, cathodic sweeps of CV curves are not completely symmetric to their corresponding anodic sweeps, which depict the quasi-reversible rate kinetics of the redox reactions **(Fig. 6C)**. Factors like polarization during faradaic redox reaction and ohmic resistance due to electrolyte diffusion into the porous electrode kinetically limit the reversibility for the positive and negative sweeps. The change in CV shape and shift in peak potential with an increase in the scan rate

indicates the low electrochemical polarization and high-power characteristics of electrode material [59]. The electrochemical reaction involved in the energy storage mechanism (Ni^{2+}/Ni^{3+} or Fe^{3+}/Fe^{2+}) is as follows [60].

$NiFe_2O_4 + H_2O + OH^- NiOOH + 2FeOOH + e^-$
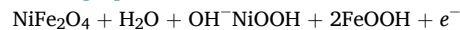
Cyclic voltammetry is an effective method to elucidate the kinetics of electrochemical reactions. The relationship between response current (I) and the scan rate (ν) is given as [61],

$$I = i_{capacitive} + i_{diffusion} = a\nu^b \tag{1}$$

where "a" and "b" are adjustable parameters and measured current 'I' at a fixed potential follows a power-law relationship with the scan rate (ν). A plot of the logarithm of (I_{pa}) v/s logarithm of (ν) of CV curves for the

P.D. Patil et al.

Journal of Energy Storage 40 (2021) 102821

MOF derived NFO500 electrode is shown in **Fig. 6D**. The $b = 0.5$ implies diffusion reaction [62] whereas $b = 1$ suggests surface charge transfer reaction between electrode and electrolyte [63]. For NFO500, the value of "*b*" was found to be 0.89, which reveals the significant contribution from capacitive behavior governed by the surface redox process. Capacitive behaviours of MOF derived NFO460, NFO500, and NFO550 electrodes were studied using the GCD technique at a current density of 0.25 A g^{-1} (**Fig. 7A**). All the GCD curves are nonlinear with well-defined charge and discharge plateaus indicating the typical faradaic behavior [64]. Noticeably, the discharge time for MOF derived NFO500 is higher than that for NFO550 and NFO460, indicating potentially excellent electrochemical performance [65].

Specific capacitance from the galvanostatic charge-discharge curve is calculated using the equation,

$$C_s = \frac{I \int V\, dt}{m\left(V_f - V_i\right)^2} \qquad (2)$$

where '*I*' denotes current intensity, '$\int Vdt$' represents the area under the charge-discharge curve, '*m*' is mass, '$(V_f - V_i)^{2\prime}$' indicates potential window, and 'Δt' is discharge time. The specific energy (E) in Wh kg^{-1} and specific power (P) in W kg^{-1} are calculated from the following equations [66],

$$E = 0.5 \times \frac{C_s\left(V_f - V_i\right)^2}{3.6} \qquad (3)$$

$$P = \frac{3600 \times E}{\Delta t} \qquad (4)$$

Taking advantage of large discharge time, MOF derived NFO500 shows a specific capacitance of 833 F g^{-1} at a current density of 0.25 A g^{-1}. The specific capacitance of NFO460 and NFO550 are 340 and 459 F g^{-1} at 0.25 A g^{-1}, respectively. The high specific capacitance of NFO500 compared to other electrodes may be attributed to a mesh-like structure that allowed electrolyte OH$^-$ ions to penetrate the electrode completely [67]. The decreased specific capacitance for NFO550 can be ascribed to the particle aggregation at the higher annealing temperature as observed in the SEM image. While in the case of NFO460, underdeveloped agglomerated threads hinder the open space for electrolyte transportation which may have resulted in low capacitance. The **Fig. 7B** shows GCD curves of MOF derived NFO500 at various current densities of 0.25, 0.50, 0.75, and 1 A g^{-1}. The discharge curves of NFO500 deviates from linearity, indicating pseudocapacitive type charge storage characteristics of electrodes [68]. There is no significant voltage drop (IR drop) during the discharge process, indicating that the internal resistance of the electrode is relatively small [69]. The specific capacitances calculated from the GCD curves as a function of the current density are shown in **Fig. 7C**. The specific capacitances of MOF derived NFO500 are calculated as 833, 648, 642 and 386 F g^{-1} at 0.25, 0.50, 0.75 and 1 A g^{-1}, respectively. The specific capacitance decreases with an increase in current densities due to the decrease in access to electrolyte ions into the electrode material's inner surface. The specific energy and the specific power of the NFO500 electrode are calculated using Eqs. (3) and 4 and are shown in the Ragone plot (**Fig. 7D**). The calculated specific capacitance, specific energy, and specific power at different current densities are presented in **Table 1**. The calculated electrochemical results of the NFO500 electrode are compared with previous reports (**Table 2**).
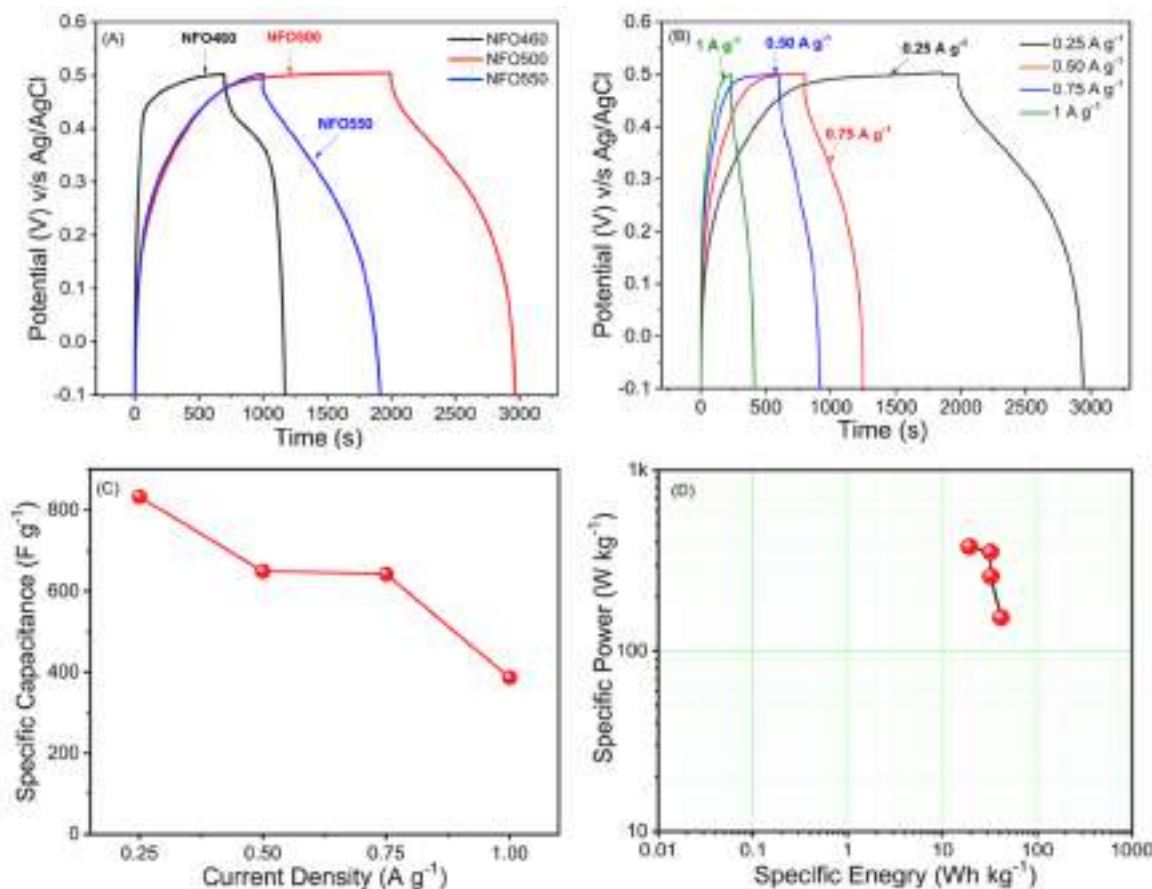
Fig. 7. (A) Galvanostatic charge-discharge (GCD) curves of MOF derived NFO460, NFO500, and NFO550 at 0.25 A g^{-1}. (B) Galvanostatic charge-discharge (GCD) curves of MOF derived NFO500 at 0.25, 0.50, 0.75, and 1 A g^{-1} current densities. (C) The specific capacitance of NFO500 against different current densities. (D) Ragone plot of MOF derived NFO500.

Table 1

Specific capacitance, specific energy, and specific power at different current densities calculated from the charge-discharge profile of MOF derived NFO500 electrode.

Current Density ($A\ g^{-1}$)	Specific Capacitance ($F\ g^{-1}$)	Specific Energy ($Wh\ kg^{-1}$)	Specific Power ($W\ kg^{-1}$)
0.25	833	42	154
0.50	648	32	259
0.75	642	32	352
1	386	19	377

Electrochemical impedance spectroscopy (EIS) measurements can be used to quantify electrical resistance, which is an important parameter of a supercapacitor electrode. The Nyquist plot of MOF derived NFO500 electrode in a frequency range from 0.01 Hz to 600 kHz is presented in **Fig. 8A**. It is showing resistive behavior (blocking) at higher frequencies [83] and an almost vertical line (ideal capacitive behavior) at lower frequencies [84]. The charge transfer resistance (R_{ct}) in the electro-chemical reaction process is represented by the diameter of the semi-circle at high frequencies. For the NFO500 electrode, R_{ct} is determined to be 2.7 Ω cm^{-2}. The electrode possesses low charge transfer resistance indicating excellent ionic conductivity. The straight line at lower frequencies represents low Warburg resistance (W), i.e., low ion diffusion resistance of the electrolyte in the electrode. It may be a result in faster faradaic charge transfer during the electrochemical process [65]. Inset shows the Randles circuit used for fitting the experimental impedance data for MOF derived NFO500 in the corresponding electrolyte solution. The equivalent circuit consists of solution resistance R_s, faradaic charge transfer resistance R_{ct}, Warburg impedance W, and constant phase element CPE. W represents the resistance in the diffusion process and access of electrolyte ions within the electrode [85]. CPE is responsible for the electric double-layer capacitance at the electrode-electrolyte interface (Pseudocapacitance often occurs alongside double-layer capacitance) [57]. From Randle's equivalent circuit model, the R_{ct} of NFO500 was found to be approximately 2 Ω cm^{-2} demonstrating the small charge transfer resistance. The specific capacitance of the super-capacitor is strongly reliant on the efficiency of ion diffusion and charge transport in the reaction [26].

The cycling performance is an important parameter for the application of a supercapacitor. GCD measurements were repeated for 3000 consecutive cycles at a current density of 3 A g^{-1} in 1 M KOH to investigate the cyclic stability of MOF derived NFO500 electrode **(Fig. 8B)**. NFO500 electrode retains 74% of its initial capacity after 3000 charge-discharge cycles with 84% coulombic efficiency. The symmetry of charge-discharge curves was consistent even after 3000 cycles without any IR drop, indicating good cycling stability.

Table 2

Comparison of the capacitance, cyclic stability, specific energy, and specific power of MOF derived NFO500 electrode with the relevant literature.

Sr. No.	Material	Morphology	Specific Capacitance	Cyclic Stability	Specific Energy	Specific Power	Ref.
1	CuFeS$_2$	Nanoflakes	219 F g^{-1} at 1 A g^{-1}	94% over 6000 cycles	16 Wh kg^{-1}	1146 W kg^{-1}	[70]
2	MnOx/N-doped carbon/MnO$_2$	Rods	284.9 F g^{-1} at 0.125 A g^{-1}	89.5% after 5000 cycles	16.8 Wh kg^{-1}	499 W kg^{-1}	[71]
3	NiCoS/CC	Nanosheet arrays	1653 F g^{-1} at 1 A g^{-1}	84% after 3000 cycles	40 Wh kg^{-1}	379 W kg^{-1}	[72]
4	Ni-Co-MOF/GO	Chestnut-like structure	447.2 F g^{-1} at 1 A g^{-1}	99.6% after 300 cycles	–	–	[73]
5	[Ag$_3$(BTC)(IM)]•H$_2$O	3D Spongy network structure	817.1 F g^{-1} at 1 A g^{-1}	75.01% after 5000 cycles	113.5 Wh kg^{-1}	–	[74]
6	NCS/PIn composites	Hemisphere	397 F g^{-1} at 1 A g^{-1}	–	13.7 Wh kg^{-1}	254 W kg^{-1}	[75]
7	NiFe$_2$O$_4$	Sheet-like structure	240.9 F g^{-1} at 1 A g^{-1}	128% after 2000 cycles	10.15 Wh kg^{-1}	140 W kg^{-1}	[76]
8	NiFe$_2$O$_4$	Nanoflakes	342 F g^{-1} at 0.833 A g^{-1}	–	–	–	[77]
9	NiFe$_2$O$_4$	Octahedral Nanocrystals	562.1 F g^{-1} at 4 A g^{-1}	80.3% after 1500 cycles	34.91 Wh kg^{-1}	1100 W kg^{-1}	[78]
10	NiFe$_2$O$_4$/MoS$_2$	Nanoparticle on nanosheets	506 F g^{-1} at 1 A g^{-1}	90.7% after 3000 cycles	–	–	[79]
11	PEDOT-NiFe$_2$O$_4$	Nanoparticles	251 F g^{-1} at ±1 mA cm^{-2}	–	34.86 Wh kg^{-1}	–	[10]
12	NiFe$_2$O$_4$/Graphene	Nanosheets	464.1 F g^{-1} at 1 A g^{-1}	140% after 5000 cycles	7.39 Wh kg^{-1}	7000 W kg^{-1}	[80]
13	rGO—NiFe$_2$O$_4$	–	345.0 F g^{-1} at 1 A g^{-1}	–	–	–	[81]
14	rGO—NiFe$_2$O$_4$	Nanoparticles	215.7 F g^{-1} at 0.5 A g^{-1}	89.4% after 10,000 cycles	–	–	[82]
15	MOF derived NiFe$_2$O$_4$	Mesh-like structure	833 F g^{-1} at 0.25 A g^{-1}	73% after 700 cycles	42 Wh kg^{-1}	154 W kg^{-1}	**This Work**
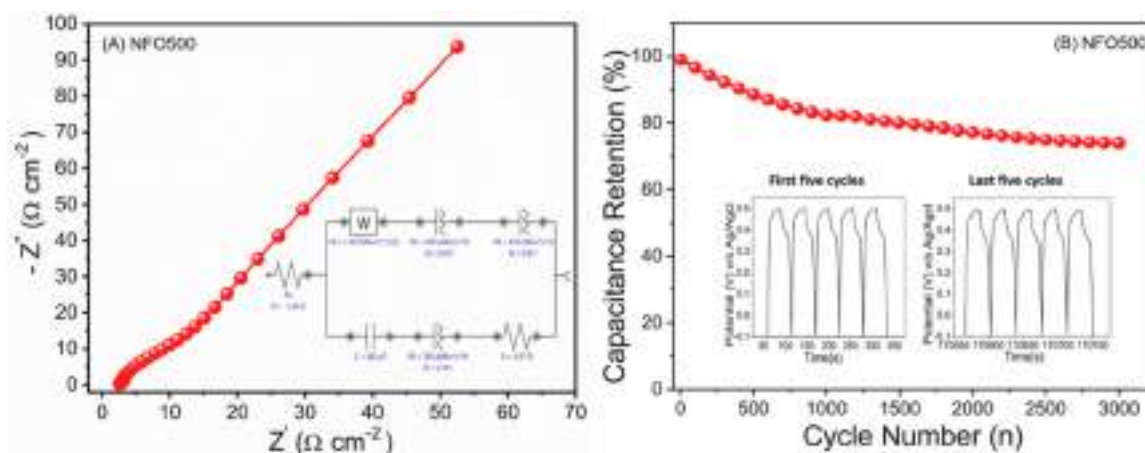
Fig. 8. (A) Nyquist plot (inset show equivalent fitted circuit), and (B) Plot of capacitance retention versus cycle number of NFO500 electrode.

4. Conclusions

MOF derived $NiFe_2O_4$ (NFO) of different morphologies were synthesized by the solvothermal method and subsequent annealing. Annealing temperature played a crucial role in determining the morphology of the samples. Different morphologies such as threads, mesh-like structures, and grains were achieved at annealing temperatures of 460 °C, 500 °C, and 550 °C, respectively. The MOF derived NFO obtained by annealing at 500 °C (NFO500) contains Ni^{2+}, Fe^{2+}, and Fe^{3+} states with NiO impurities and some carbon derivatives due to the incomplete decomposition of the organic ligand. NFO500 rhombus nanoplates with interconnected mesh-like structure significantly improved the electrochemical performance of the supercapacitor. Mesoporous nature of NFO500 with a surface area of 38.17 $m^2\ g^{-1}$ aids in shortening charge transfer pathways and improving the active sites for reversible surface redox reactions. MOF derived NFO500 exhibited a high specific capacitance of 833 F g^{-1} at 0.25 A g^{-1} compared to that of NFO460 and NFO550 in 1 M KOH electrolyte solution. NFO500 electrode also displayed excellent electrochemical performances in terms of specific energy and specific power (42 Wh kg^{-1} at 154 W kg^{-1}). Cyclic stability study of NFO500 electrode revealed 74% capacitance retention with 84% coulombic efficiency after 3000 cycles at 3 A g^{-1}. The superior supercapacitive performance of NFO500 compared to other electrodes is attributed to better charge transfer ability and the mesh-like structure, which allowed electrolyte ions to penetrate the electrode completely. This study may pave the way to tailor the morphologies of MOF derived nanostructures for supercapacitor applications.

Credit author statement

Prashant Patil: Conceptualization, Methodology and Experimental Supervision.

Priyanka Patil and Shamal Shingte: Data interpretation, Writing-Original draft preparation.

Vijay Karade, Jin Hyeok Kim, Sarfraj Mujawar, and Amar Patil: Materials characterizations

Tukaram Dongale and Amar Patil: Reviewing and Editing

Declaration of Competing Interest

The authors declare that they have no known competing financial interests or personal relationships that could have appeared to influence the work reported in this paper.

Acknowledgments

References

[1] S.R.C. Vivekchand, Chandra C.Sekhar S. Rout, K.S. Subrahmanyam, Graphene-Based Electrochemical Supercapacitors, J. Chem. Sci. 120 (2008) 9–13, https://doi.org/10.1016/B978-0-12-814523-4.00009-5.

[2] G.A. Snook, P. Kao, A.S. Best, Conducting-polymer-based supercapacitor devices and electrodes, J. Power Sources. 196 (2011) 1–12, https://doi.org/10.1016/j.jpowsour.2010.06.084.

[3] S.M. Nikam, A. Sharma, M. Rahaman, A.M. Teli, S.H. Mujawar, D.R.T. Zahn, P. S. Patil, S.C. Sahoo, G. Salvan, P.B. Patil, Pulsed laser deposited $CoFe_2O_4$ thin films as supercapacitor electrodes, RSC Adv. 10 (2020) 19353–19359, https://doi.org/10.1039/d0ra02564j.

[4] N. Kumar, A. Kumar, G.M. Huang, W.W. Wu, T.Y. Tseng, Facile synthesis of mesoporous $NiFe_2O_4$/CNTs nanocomposite cathode material for high performance asymmetric pseudocapacitors, Appl. Surf. Sci. 433 (2018) 1100–1112, https://doi.org/10.1016/j.apsusc.2017.10.095.

[5] M.S. Park, J. Kim, K.J. Kim, J.W. Lee, J.H. Kim, Y. Yamauchi, Porous nanoarchitectures of spinel-type transition metal oxides for electrochemical energy storage systems, Phys. Chem. Chem. Phys. 17 (2015) 30963–30977, https://doi.org/10.1039/c5cp05936d.

[6] F. Cao, G.X. Pan, X.H. Xia, P.S. Tang, H.F. Chen, Synthesis of hierarchical porous NiO nanotube arrays for supercapacitor application, J. Power Sources. 264 (2014) 161–167, https://doi.org/10.1016/j.jpowsour.2014.04.103.

[7] L. Zhang, D. Shi, T. Liu, M. Jaroniec, J. Yu, Nickel-based materials for supercapacitors, Mater. Today. 25 (2019) 35–65, https://doi.org/10.1016/j.mattod.2018.11.002.

[8] L. Feng, Y. Zhu, H. Ding, C. Ni, Recent progress in nickel based materials for high performance pseudocapacitor electrodes, J. Power Sources. 267 (2014) 430–444, https://doi.org/10.1016/j.jpowsour.2014.05.092.

[9] S.L. Kuo, N.L. Wu, Electrochemical capacitor of $MnFe_2O_4$ with NaCl electrolyte, Electrochem. Solid-State Lett. 8 (2005) 495–499, https://doi.org/10.1149/1.2008847.

[10] P. Sen, A. De, Electrochemical performances of poly(3,4-ethylenedioxythiophene)-$NiFe_2O_4$ nanocomposite as electrode for supercapacitor, Electrochim. Acta. 55 (2010) 4677–4684, https://doi.org/10.1016/j.electacta.2010.03.077.

[11] R.R. Salunkhe, Y.V. Kaneti, Y. Yamauchi, Metal-Organic Framework-Derived Nanoporous Metal Oxides toward Supercapacitor Applications: progress and Prospects, ACS Nano 11 (2017) 5293–5308, https://doi.org/10.1021/acsnano.7b02796.

[12] K.M. Choi, H.M. Jeong, J.H. Park, Y.B. Zhang, J.K. Kang, O.M. Yaghi, Supercapacitors of nanocrystalline metal-organic frameworks, ACS Nano 8 (2014) 7451–7457, https://doi.org/10.1021/nn5027092.

[13] Y. Te Liao, V.C. Nguyen, N. Ishiguro, A.P. Young, C.K. Tsung, K.C.W. Wu, Engineering a homogeneous alloy-oxide interface derived from metal-organic frameworks for selective oxidation of 5-hydroxymethylfurfural to 2,5-furandicarboxylic acid, Appl. Catal. B Environ. (2020) 270, https://doi.org/10.1016/j.apcatb.2020.118805.

[14] Y. Te Liao, B.M. Matsagar, K.C.W. Wu, Metal-Organic Framework (MOF)-Derived Effective Solid Catalysts for Valorization of Lignocellulosic Biomass, ACS Sustain. Chem. Eng. 6 (2018) 13628–13643, https://doi.org/10.1021/acssuschemeng.8b03683.

[15] Y.C. Liu, L.H. Yeh, M.J. Zheng, K.C.W. Wu, Highly selective and high-performance osmotic power generators in subnanochannel membranes enabled by metal-organic frameworks, Sci. Adv. 7 (2021), https://doi.org/10.1126/sciadv.abe9924.

[16] H. Konnerth, B.M. Matsagar, S.S. Chen, M.H.G. Prechtl, F.K. Shieh, K.C.W. Wu, Metal-organic framework (MOF)-derived catalysts for fine chemical production, Coord. Chem. Rev. 416 (2020), 213319, https://doi.org/10.1016/j.ccr.2020.213319.

[17] Y. Li, Y. Xu, W. Yang, W. Shen, H. Xue, H. Pang, MOF-Derived Metal Oxide Composites for Advanced Electrochemical Energy Storage, Small 14 (2018) 1–24, https://doi.org/10.1002/smll.201704435.

[18] L. Sun, C.H. Hendon, S.S. Park, Y. Tulchinsky, R. Wan, F. Wang, A. Walsh, M. Dincǎ, Is iron unique in promoting electrical conductivity in MOFs? Chem. Sci. 8 (2017) 4450–4457, https://doi.org/10.1039/c7sc00647k.

[19] S. Wu, J. Liu, H. Wang, H. Yan, A review of performance optimization of MOF-derived metal oxide as electrode materials for supercapacitors, Int. J. Energy Res. 43 (2019) 697–716, https://doi.org/10.1002/er.4232.

[20] A. Mahmood, R. Zou, Q. Wang, W. Xia, H. Tabassum, B. Qiu, R. Zhao, Nanostructured electrode materials derived from metal-organic framework xerogels for high-energy-density asymmetric supercapacitor, ACS Appl. Mater. Interfaces. 8 (2016) 2148–2157, https://doi.org/10.1021/acsami.5b10725.

[21] H. Yu, H. Fan, B. Yadian, H. Tan, W. Liu, H.H. Hng, Y. Huang, Q. Yan, General Approach for MOF-Derived Porous Spinel AFe_2O_4 Hollow Structures and Their Superior Lithium Storage Properties, ACS Appl. Mater. Interfaces. 7 (2015) 26751–26757, https://doi.org/10.1021/acsami.5b08741.

[22] X. Xiao, L. Zou, H. Pang, Q. Xu, Synthesis of micro/nanoscaled metal-organic frameworks and their direct electrochemical applications, Chem. Soc. Rev. 49 (2020) 301–331, https://doi.org/10.1039/c7cs00614d.

[23] D.Y. Lee, D.V. Shinde, E.K. Kim, W. Lee, I.W. Oh, N.K. Shrestha, J.K. Lee, S.H. Han, Supercapacitive property of metal-organic-frameworks with different pore dimensions and morphology, Microporous Mesoporous Mater. 171 (2013) 53–57, https://doi.org/10.1016/j.micromeso.2012.12.039.

[24] A. Indra, T. Song, U. Paik, Metal Organic Framework Derived Materials: progress and Prospects for the Energy Conversion and Storage, Adv. Mater. 30 (2018) 1–25, https://doi.org/10.1002/adma.201705146.

[25] Y. Lü, W. Zhan, Y. He, Y. Wang, X. Kong, Q. Kuang, Z. Xie, L. Zheng, MOF-templated synthesis of porous Co_3O_4 concave nanocubes with high specific surface area and their gas sensing properties, ACS Appl. Mater. Interfaces. 6 (2014) 4186–4195, https://doi.org/10.1021/am405858v.

[26] M.K. Wu, C. Chen, J.J. Zhou, F.Y. Yi, K. Tao, L. Han, MOF–derived hollow double–shelled NiO nanospheres for high–performance supercapacitors, J. Alloys Compd. 734 (2018) 1–8, https://doi.org/10.1016/j.jallcom.2017.10.171.

[27] Q. F., S.Q. Siru Chen, Ming M. Xue*, Yanqiang Y. Li, Ying Y. Pan, Liangkui L. Zhu, Daliang D. Zhang, Porous $ZnCo_2O_4$ nanoparticles derived from a new mixed-metal organic framework for supercapacitors, Inorg. Chem. 2.2 (2015) 177–183, https://doi.org/10.1039/C4QI00167B.

[28] S.W. Oh, H.J. Bang, Y.C. Bae, Y.K. Sun, Effect of calcination temperature on morphology, crystallinity and electrochemical properties of nano-crystalline metal oxides (Co_3O_4, CuO, and NiO) prepared via ultrasonic spray pyrolysis, J. Power Sources. 173 (2007) 502–509, https://doi.org/10.1016/j.jpowsour.2007.04.087.

[29] N.BudhirajaB. Sapna, V. Kumar, S.K. Singh, Tailoring the Structural, Optical and Magnetic Properties of NiFe$_2$O$_4$ by Varying Annealing Temperature, J. Supercond. Nov. Magn. 31 (2018) 2647–2654, https://doi.org/10.1007/s10948-017-4524-z.

[30] H. Zhang, L. Zhang, J. Deng, Y. Han, X. Li, Fabrication of porous Co$_3$O$_4$ with different nanostructures by solid-state thermolysis of metal–organic framework for supercapacitors, J. Mater. Sci. 53 (2018) 8474–8482, https://doi.org/10.1007/s10853-018-2157-z.

[31] S.M. Patil, S.R. Shingte, V.C. Karade, J.H. Kim, R.M. Kulkarni, A.D. Chougale, P. B. Patil, Electrochemical performance of magnetic nanoparticle-decorated reduced graphene oxide (MRGO) in various aqueous electrolyte solutions, J. Solid State Electrochem. 25.3 (2020) 927–938, https://doi.org/10.1007/s10008-020-04866-x.

[32] Y. Jiao, J. Pei, C. Yan, D. Chen, Y. Hu, G. Chen, Layered nickel metal-organic framework for high performance alkaline battery-supercapacitor hybrid devices, J. Mater. Chem. A. 4 (2016) 13344–13351, https://doi.org/10.1039/c6ta05384j.

[33] J.M. a Wenlong Zhen a, Enhancing catalytic activity and stability for CO$_2$ methanation on Ni@MOF-5 via controlling active species dispersion, J. ChemCommChemComm. 51.9 (2014) 1728–1731, https://doi.org/10.1039/C4CC08733J.

[34] E.K. Nyutu, W.C. Conner, S.M. Auerbach, C.H. Chen, S.L. Suib, Ultrasonic nozzle spray in situ mixing and microwave-assisted preparation of nanocrystalline spinel metal oxides: nickel ferrite and zinc aluminate, J. Phys. Chem. C. 112 (2008) 1407–1414, https://doi.org/10.1021/jp075647l.

[35] A.T. Raghavender, K. Zadro, D. Pajic, Z. Skoko, N. Biliškov, Effect of grain size on the Néel temperature of nanocrystalline nickel ferrite, Mater. Lett. 64 (2010) 1144–1146, https://doi.org/10.1016/j.matlet.2010.02.031.

[36] D. Ma, M. Lv, Y. Shen, Y. Zhu, F. Wang, X. Zhang, Fabrication of Porous Mesh-Like FeCo$_2$S$_4$ Nanosheet Arrays on Ni Foam for High Performance all Solid-State Supercapacitors and Water Splitting, ChemistrySelect 4 (2019) 1879–1889, https://doi.org/10.1002/slct.201803107.

[37] D.P. Dubal, W.B. Kim, C.D. Lokhande, Surfactant assisted electrodeposition of MnO$_2$ thin films: improved supercapacitive properties, J. Alloys Compd. 509 (2011) 10050–10054, https://doi.org/10.1016/j.jallcom.2011.08.029.

[38] S.V. Bhosale, P.S. Ekambe, S.V. Bhoraskar, V.L. Mathe, Effect of surface properties of NiFe$_2$O$_4$ nanoparticles synthesized by dc thermal plasma route on antimicrobial activity, Appl. Surf. Sci. 441 (2018) 724–733, https://doi.org/10.1016/j.apsusc.2018.01.220.

[39] A. Hao, M. Ismail, S. He, N. Qin, W. Huang, J. Wu, D. Bao, Ag-NPs doping enhanced resistive switching performance and induced changes in magnetic properties of NiFe$_2$O$_4$ thin films, RSC Adv 7 (2017) 46665–46677, https://doi.org/10.1039/c7ra08756j.

[40] M. Fu, Z. Qiu, W. Chen, Y. Lin, H. Xin, B. Yang, H. Fan, C. Zhu, J. Xu, NiFe$_2$O$_4$ porous nanorods/graphene composites as high-performance anode materials for lithium-ion batteries, Electrochim. Acta. 248 (2017) 292–298, https://doi.org/10.1016/j.electacta.2017.07.027.

[41] W.J. Dang, Y.Q. Shen, M. Lin, H. Jiao, L. Xu, Z.L. Wang, Noble-metal-free electrocatalyst based on a mixed CoNi metal-organic framework for oxygen evolution reaction, J. Alloys Compd. 792 (2019) 69–76, https://doi.org/10.1016/j.jallcom.2019.03.399.

[42] L. Marchetti, F. Miserque, S. Perrin, M. Pijolat, XPS study of Ni-base alloys oxide films formed in primary conditions of pressurized water reactor, Surf. Interface Anal. 47 (2015) 632–642, https://doi.org/10.1002/sia.5757.

[43] S. Megala, S. Prabhu, S. Harish, M. Navaneethan, S. Sohila, R. Ramesh, Enhanced photocatalytic dye degradation activity of carbonate intercalated layered Zn, ZnNi and ZnCu hydroxides, Appl. Surf. Sci. 481 (2019) 385–393, https://doi.org/10.1016/j.apsusc.2019.03.091.

[44] J. Jiang, H. Gao, S. Lu, X. Zhang, C.Y. Wang, W.K. Wang, H.Q. Yu, Ni-Pd core-shell nanoparticles with Pt-like oxygen reduction electrocatalytic performance in both acidic and alkaline electrolytes, J. Mater. Chem. A. 5 (2017) 9233–9240, https://doi.org/10.1039/c7ta01754e.

[45] Y. Xia, B. Wang, G. Wang, X. Liu, H. Wang, MOF-Derived Porous Ni$_x$Fe$_{3-x}$O$_4$ Nanotubes with Excellent Performance in Lithium-Ion Batteries, ChemElectroChem 3 (2016) 299–308, https://doi.org/10.1002/celc.201500419.

[46] Z.J. Jiang, S. Cheng, H. Rong, Z. Jiang, J. Huang, General synthesis of MFe2O4/carbon (M = Zn, Mn, Co, Ni) spindles from mixed metal organic frameworks as high performance anodes for lithium ion batteries, J. Mater. Chem. A. 5 (2017) 23641–23650. https://doi.org/10.1039/c7ta07097g.

[47] X. Zhang, B. Zhang, S. Liu, H. Kang, W. Kong, S. Zhang, Y. Shen, B. Yang, RGO modified Ni doped FeOOH for enhanced electrochemical and photoelectrochemical water oxidation, Appl. Surf. Sci. 436 (2018) 974–980, https://doi.org/10.1016/j.apsusc.2017.12.078.

[48] Y. Zhang, C. Jia, Q. Wang, Q. Kong, G. Chen, H. Guan, C. Dong, MOFs-derived porous NiFe$_2$O$_4$ nano-octahedrons with hollow interiors for an excellent toluene gas sensor, Nanomaterials 9 (2019) 1059, https://doi.org/10.3390/nano9081059.

[49] X. Zhang, N. Qu, S. Yang, Q. Fan, D. Lei, A. Liu, X. Chen, Shape-controlled synthesis of Ni-based metal-organic frameworks with albizia flower-like spheres@ nanosheets structure for high performance supercapacitors, J. Colloid Interface Sci. 575 (2020) 347–355, https://doi.org/10.1016/j.jcis.2020.04.127.

[50] W. Lu, X. Wu, Ni-MOF nanosheet arrays: efficient non-noble-metal electrocatalysts for non-enzymatic monosaccharide sensing, New J. Chem. 42 (2018) 3180–3183, https://doi.org/10.1039/c7nj04754a.

[51] Y. Bin Liu, L.Y. Lin, Y.Y. Huang, C.C. Tu, Investigation of the electroactive capability for the supercapacitor electrode with cobalt oxide rhombus nanopillar and nanobrush arrays, J. Power Sources. 315 (2016) 23–34, https://doi.org/10.1016/j.jpowsour.2016.03.035.

[52] S. Wang, H. Gao, X. Yu, S. Tang, Y. Wang, L. Fang, X. Zhao, J. Li, L. Yang, W. Dang, Nanostructured SrTiO$_3$ with different morphologies achieved by mineral acid-assisted hydrothermal method with enhanced optical, electrochemical, and photocatalytic performances, J. Mater. Sci. Mater. Electron. 31 (2020) 17736–17754, https://doi.org/10.1007/s10854-020-04328-0.

[53] S.S. Shinde, C.H. Lee, A. Sami, D.H. Kim, S.U. Lee, J.H. Lee, Scalable 3-D Carbon Nitride Sponge as an Efficient Metal-Free Bifunctional Oxygen Electrocatalyst for Rechargeable Zn-Air Batteries, ACS Nano 11 (2017) 347–357, https://doi.org/10.1021/acsnano.6b05914.

[54] S.A. Jadhav, S.B. Somvanshi, M.V. Khedkar, S.R. Patade, K.M. Jadhav, Magneto-structural and photocatalytic behavior of mixed Ni–Zn nano-spinel ferrites: visible light-enabled active photodegradation of rhodamine B, J. Mater. Sci. Mater. Electron. 31 (2020) 11352–11365, https://doi.org/10.1007/s10854-020-03684-1.

[55] D. Lim, H. Kong, N. Kim, C. Lim, W.S. Ahn, S.H. Baeck, Oxygen-Deficient NiFe$_2$O$_4$ Spinel Nanoparticles as an Enhanced Electrocatalyst for the Oxygen Evolution Reaction, ChemNanoMat 5 (2019) 1296–1302, https://doi.org/10.1002/cnma.201900231.

[56] A.M. Patil, X. An, S. Li, X. Yue, X. Du, A. Yoshida, X. Hao, A. Abudula, G. Guan, Fabrication of three-dimensionally heterostructured rGO/WO$_3$•0•5H$_2$O/Cu$_2$S electrodes for high-energy solid-state pouch-type asymmetric supercapacitor, Chem. Eng. J. 403 (2021) 126411, https://doi.org/10.1016/j.cej.2020.126411.

[57] K. Wang, Z. Wang, X. Wang, X. Zhou, Y. Tao, H. Wu, Flexible long-chain-linker constructed Ni-based metal-organic frameworks with 1D helical channel and their pseudo-capacitor behavior studies, J. Power Sources. 377 (2018) 44–51, https://doi.org/10.1016/j.jpowsour.2017.11.087.

[58] M. Sethi, U.S. Shenoy, S. Muthu, D.K. Bhat, Facile solvothermal synthesis of NiFe$_2$O$_4$ nanoparticles for high-performance supercapacitor applications, Front. Mater. Sci. 14 (2020) 120–132, https://doi.org/10.1007/s11706-020-0499-3.

[59] H. Adhikari, M. Ghimire, C.K. Ranaweera, S. Bhoyate, R.K. Gupta, J. Alam, S. R. Mishra, Synthesis and electrochemical performance in presence of hydrothermally synthesized Co$_3$O$_4$ nanostructured particles in presence of urea, J. Alloys Compd. 708 (2017) 628–638, https://doi.org/10.1016/j.jallcom.2017.03.056.

[60] B. Mordina, R. Kumar, N.S. Neeraj, A.K. Srivastava, D.K. Setua, A. Sharma, Binder free high performance hybrid supercapacitor device based on nickel ferrite nanoparticles, J. Energy Storage. 31 (2020), 101677, https://doi.org/10.1016/j.est.2020.101677.

[61] Y. Wang, Y. Song, Y. Xia, Electrochemical capacitors: mechanism, materials, systems, characterization and applications, Chem. Soc. Rev. 45 (2016) 5925–5950, https://doi.org/10.1039/c5cs00580a.

[62] A. Ray, A. Roy, P. Sadhukhan, S.R. Chowdhury, P. Maji, S.K. Bhattacharya, S. Das, Electrochemical properties of TiO$_2$ -V$_2$O$_5$ nanocomposites as a high performance supercapacitors electrode material, Appl. Surf. Sci. 443 (2018) 581–591, https://doi.org/10.1016/j.apsusc.2018.02.277.

[63] T.S. Mathis, N. Kurra, X. Wang, D. Pinto, P. Simon, Y. Gogotsi, Energy Storage Data Reporting in Perspective—Guidelines for Interpreting the Performance of Electrochemical Energy Storage Systems, Adv. Energy Mater. 9 (2019) 1–13, https://doi.org/10.1002/aenm.201902007.

[64] K. Xu, S. Ma, Y. Shen, Q. Ren, J. Yang, X. Chen, J. Hu, CuCo$_2$O$_4$ nanowire arrays wrapped in metal oxide nanosheets as hierarchical multicomponent electrodes for supercapacitors, Chem. Eng. J. 369 (2019) 363–369, https://doi.org/10.1016/j.cej.2019.03.079.

[65] J. Shen, P. Wang, H. Jiang, H. Wang, B.G. Pollet, R. Wang, S. Ji, MOF derived graphitic carbon nitride/oxygen vacancies-rich zinc oxide nanocomposites with enhanced supercapacitive performance, Ionics (Kiel) 26 (2020) 5155–5165, https://doi.org/10.1007/s11581-020-03597-3.

[66] B. Pandit, D.P. Dubal, B.R. Sankapal, Large scale flexible solid state symmetric supercapacitor through inexpensive solution processed V$_2$O$_5$ complex surface architecture, Electrochim. Acta. 242 (2017) 382–389, https://doi.org/10.1016/j.electacta.2017.05.010.

[67] I.W. Fathona, A. Yabuki, Mesh-like thin-film electrodes of manganese oxide with high specific capacitance synthesized via thermal decomposition of manganese formate-amine complexed ink, Mater. Res. Bull. 112 (2019) 346–353, https://doi.org/10.1016/j.materresbull.2019.01.004.

[68] D. Ghosh, S. Giri, C.K. Das, Preparation of CTAB-assisted hexagonal platelet Co (OH)$_2$/graphene hybrid composite as efficient supercapacitor electrode material, ACS Sustain. Chem. Eng. 1 (2013) 1135–1142, https://doi.org/10.1021/sc400055z.

[69] L. Shao, Q. Wang, Z. Ma, Z. Ji, X. Wang, D. Song, Y. Liu, N. Wang, A high-capacitance flexible solid-state supercapacitor based on polyaniline and Metal-Organic Framework (UiO-66) composites, J. Power Sources. 379 (2018) 350–361, https://doi.org/10.1016/j.jpowsour.2018.01.028.

[70] P. Rupa Ranjani, P.M. Anjana, R.B. Rakhi, Solvothermal synthesis of CuFeS$_2$ nanoflakes as a promising electrode material for supercapacitors, J. Energy Storage. 33 (2021) 102063, https://doi.org/10.1016/j.est.2020.102063.

[71] K. Wang, K. Wang, R. Bi, Y. Chu, Z. Wang, H. Wu, H. Pang, Controllable synthesis and electrochemical capacitor performance of MOF-derived MnO: x/N-doped carbon/MnO$_2$ composites, Inorg. Chem. Front. 6 (2019) 2873–2884, https://doi.org/10.1039/c9qi00596j.

[72] T. Liu, J. Liu, L. Zhang, B. Cheng, J. Yu, Journal of Materials Science & Technology Construction of nickel cobalt sulfide nanosheet arrays on carbon cloth for performance-enhanced supercapacitor, J. Mater. Sci. Technol. 47 (2020) 113–121, https://doi.org/10.1016/j.jmst.2019.12.027.

[73] J. Hong, S.J. Park, S. Kim, Synthesis and electrochemical characterization of nanostructured Ni-Co-MOF/graphene oxide composites as capacitor electrodes, Electrochim. Acta. 311 (2019) 62–71, https://doi.org/10.1016/j.electacta.2019.04.121.

[74] Q. Wang, S. Li, J. Zhang, X. Zhao, H. Feng, H. Luo, Preparation of MOFs derived nitrogen self-doped porous carbon and its electrochemical performance in mixed electrolytes, Appl. Surf. Sci. 500 (2020), 143936, https://doi.org/10.1016/j.apsusc.2019.143936.

[75] M. Majumder, R.B. Choudhary, A.K. Thakur, Hemispherical nitrogen-doped carbon spheres integrated with polyindole as high performance electrode material for supercapacitor applications, Carbon N. Y. 142 (2019) 650–661, https://doi.org/10.1016/j.carbon.2018.10.089.

[76] X. Gao, W. Wang, J. Bi, Y. Chen, X. Hao, X. Sun, J. Zhang, Morphology-controllable preparation of $NiFe_2O_4$ as high performance electrode material for supercapacitor, Electrochim. Acta. 296 (2019) 181–189, https://doi.org/10.1016/j.electacta.2018.11.054.

[77] P. Bhojane, A. Sharma, M. Pusty, Y. Kumar, S. Sen, P. Shirage, Synthesis of ammonia-assisted porous nickel ferrite ($NiFe_2O_4$) nanostructures as an electrode material for supercapacitors, J. Nanosci. Nanotechnol. 17 (2017) 1387–1392, https://doi.org/10.1166/jnn.2017.12666.

[78] M. Hua, L. Xu, F. Cui, J. Lian, Y. Huang, J. Bao, J. Qiu, Y. Xu, H. Xu, Y. Zhao, H. Li, Hexamethylenetetramine-assisted hydrothermal synthesis of octahedral nickel ferrite oxide nanocrystallines with excellent supercapacitive performance, J. Mater. Sci. 53 (2018) 7621–7636, https://doi.org/10.1007/s10853-018-2052-7.

[79] Y. Zhao, L. Xu, J. Yan, W. Yan, C. Wu, J. Lian, Y. Huang, J. Bao, J. Qiu, L. Xu, Y. Xu, H. Xu, H. Li, Facile preparation of $NiFe_2O_4/MoS_2$ composite material with synergistic effect for high performance supercapacitor, J. Alloys Compd. 726 (2017) 608–617, https://doi.org/10.1016/j.jallcom.2017.07.327.

[80] X. Gao, J. Bi, W. Wang, H. Liu, Y. Chen, X. Hao, X. Sun, R. Liu, Morphology-controllable synthesis of $NiFe_2O_4$ growing on graphene nanosheets as advanced electrode material for high performance supercapacitors, J. Alloys Compd. 826 (2020), 154088, https://doi.org/10.1016/j.jallcom.2020.154088.

[81] Z. Wang, X. Zhang, Y. Li, Z. Liu, Z. Hao, Synthesis of graphene-$NiFe_2O_4$ nanocomposites and their electrochemical capacitive behavior, J. Mater. Chem. A. 1 (2013) 6393–6399, https://doi.org/10.1039/c3ta10433h.

[82] Y.Z. Cai, W.Q. Cao, P. He, Y.L. Zhang, M.S. Cao, $NiFe_2O_4$ nanoparticles on reduced graphene oxide for supercapacitor electrodes with improved capacitance, Mater. Res. Express. 6 (2019), 105535, https://doi.org/10.1088/2053-1591/ab3fff.

[83] K. Bindu, K. Sridharan, K.M. Ajith, H.N. Lim, H.S. Nagaraja, Microwave assisted growth of stannous ferrite microcubes as electrodes for potentiometric nonenzymatic H_2O_2 sensor and supercapacitor applications, Electrochim. Acta. 217 (2016) 139–149, https://doi.org/10.1016/j.electacta.2016.09.083.

[84] L. Wang, H. Ji, S. Wang, L. Kong, X. Jiang, G. Yang, Preparation of Fe_3O_4 with high specific surface area and improved capacitance as a supercapacitor, Nanoscale 5 (2013) 3793–3799, https://doi.org/10.1039/c3nr00256j.

[85] N.K. Sidhu, A.C. Rastogi, Vertically aligned ZnO nanorod core-polypyrrole conducting polymer sheath and nanotube arrays for electrochemical supercapacitor energy storage, Nanoscale Res. Lett. 9 (2014) 1–16, https://doi.org/10.1186/1556-276X-9-453.